



Gamma-Ray Emission Revealed at the Western Edge of SNR G344.7–0.1

J. Eagle^{1,2}, S. Marchesi¹, D. Castro², M. Ajello¹, and A. Venderbasco¹

¹Department of Physics & Astronomy, Clemson University, Clemson, SC 29634, USA

²Harvard-Smithsonian Center for Astrophysics, Cambridge, MA 02138, USA

Received 2020 June 15; revised 2020 October 2; accepted 2020 October 2; published 2020 November 26

Abstract

We report on the investigation of a very high energy (VHE), Galactic γ -ray source recently discovered at >50 GeV using the Large Area Telescope (LAT) on board the Fermi Gamma-ray Space Telescope (Fermi). This object, 2FHL J1703.4–4145, displays a very hard >50 GeV spectrum with a photon index $\Gamma_\gamma \sim 1.2$ in the 2FHL catalog and, as such, is one of the most extreme sources in the 2FHL subsample of Galactic objects. A detailed analysis of the available multiwavelength data shows that this source is located on the western edge of the supernova remnant (SNR) G344.7–0.1, along with extended TeV source, HESS J1702–420. The observations and the spectral energy distribution modeling support a scenario where this γ -ray source is the byproduct of the interaction between the SNR shock and the dense surrounding medium, with escaping cosmic rays (CRs) diffusing into the dense environment and interacting with a large local cloud, generating the observed TeV emission. If confirmed, an interaction between the SNR CRs and a nearby cloud would make 2FHL J1703.4–4145 another promising candidate for efficient particle acceleration of the 2FHL Galactic sample, following the first candidate from our previous investigation of a likely shock–cloud interaction occurring on the western edge of the Vela SNR.

Unified Astronomy Thesaurus concepts: [High energy astrophysics \(1656\)](#)

1. Introduction

Efficient particle accelerators responsible for Galactic cosmic rays (CRs) are abundant in the the Milky Way, whose interactions with the ambient medium and photon fields produce energetic γ -rays. Therefore, γ -rays provide an excellent way to probe nonthermal astrophysical processes. Relativistic electrons (i.e., leptons) can produce γ -rays by nonthermal bremsstrahlung from Coulomb interactions with ions or by inverse Compton scattering (ICS) on ambient photon fields, whereas protons and heavier nuclei (i.e., hadrons) produce γ -ray emission via hadronic collisions with ambient material generating pions that then decay quickly to γ -rays. Studies of the nonthermal Galactic source population are essential to understand how and where the bulk of cosmic rays are being accelerated and to understand the mechanisms underlying very high energy (VHE; $E > 50$ GeV) emitters (Renaud 2009; Kargaltsev et al. 2013).

Several deep sky observations have been performed to study the Galactic plane in the TeV γ -ray energy band with facilities like the H.E.S.S., MAGIC, and VERITAS ground-based Cherenkov telescopes (Berlöhner et al. 2003; Ferenc & MAGIC Collaboration 2005; Holder et al. 2006; Barrio & CTA Consortium 2020). These surveys revealed that the Galactic plane is rich with TeV γ -ray emission from systems leftover from supernova explosions such as pulsar wind nebulae (PWNe) and supernova remnants (SNRs; Funk 2005; Aharonian et al. 2006; Ong 2014; Eger 2015). Recently, the Pass 8 (Atwood et al. 2013) event level reconstruction and analysis has enabled the Fermi-Large Area Telescope (LAT) to achieve similar sensitivity and coverage to the aforementioned facilities at energies above 50 GeV, reaching an average sensitivity in the plane of $\sim 2\%$ of the Crab flux (only slightly less sensitive than H.E.S.S. in this energy band; see H.E.S.S. Collaboration et al. 2018) with a localization accuracy better than $3'$ for most sources (Ackermann et al. 2016).

One breakthrough possible with Pass 8 has been the survey of the entire sky at >50 GeV reported in the 2FHL catalog

(Ackermann et al. 2016), which is composed of 360 sources. Of these objects, 103 are detected in the Galactic plane ($|b| < 10^\circ$): 38 of these have been associated with Galactic objects as their counterparts, 42 are associated with blazars, and 23 are unassociated. None of the 23 unassociated sources have the radio or optical properties of blazars, though it may still be possible to have blazars present in the subsample. A second selection criterion is applied to classify sources as Galactic in origin by considering the hardness of the γ -ray spectrum at 50 GeV, since at these energies blazars generally exhibit a soft spectrum with an average photon index of $\Gamma \sim 3.4$ in the 2FHL catalog. This is because the energy range is above the inverse Compton (IC) peak of their spectral energy distribution (SED).

Among the 23 unidentified 2FHL objects located in the Galactic plane, 12 have $\Gamma < 1.8$, and hence the number of contaminant blazars in this hard-spectrum subsample is expected to be < 1 . Thus, this subsample should be comprised of newly detected hard-spectrum Galactic objects. In Eagle et al. (2019), we report the first findings from the subsample on 2FHL J0826.1–4500, which is found to be a probable shock–cloud interaction on the western edge of the Vela SNR (hereafter referred to as Paper 1a). In this work, we focus on another object in our sample, 2FHL J1703.4–4145, which is similarly located at the western rim of a supernova remnant, SNR G344.7–0.1.

1.1. SNR G344.7–0.1

The discovery of SNR G344.7–0.1 was first reported by Clark et al. (1975) with observations at 408 and 5000 MHz. Since then, it has been established that the SNR is relatively young to middle-aged with an age estimated to be $\tau \sim 3,000$ yr and is roughly $8'$ in diameter in the radio with the brightest radio emission seen to be in the northern, central, and western regions of the remnant (Dubner et al. 1993; Whiteoak & Green 1996). Dubner et al. (1993) determined the distance of the SNR to be $d \approx 14$ kpc and in Giacani et al. (2011) it is

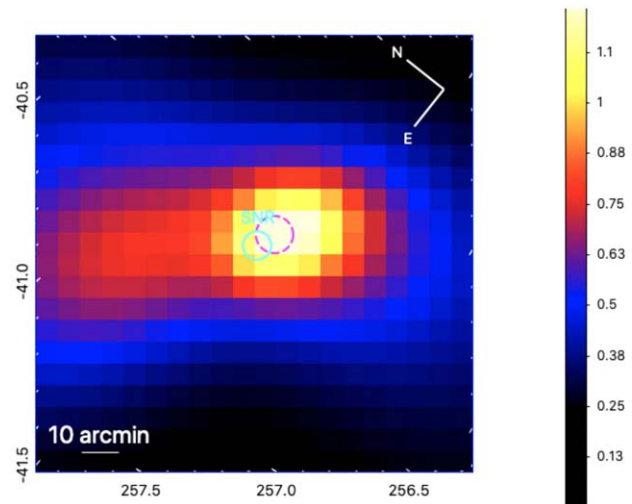
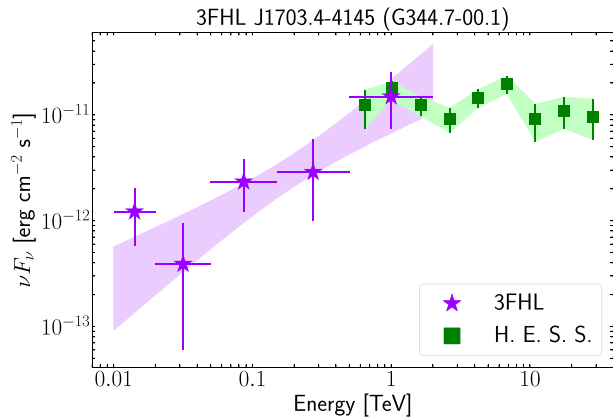


Figure 1. Left: γ -ray SED of 2FHL J1703.4–4145, using data from the 3FHL catalog (Ajello et al. 2017). Also plotted are the data from the likely TeV counterpart HESS J1702–420 (see the text; H.E.S.S. Collaboration et al. 2018). Right: an adaptively smoothed γ -ray image of the Fermi-LAT ≥ 50 GeV sky where 2FHL J1703.4–4145 is located. The source shows no significant evidence of extended emission. The count map is not background subtracted, and the 2FHL source is embedded in Galactic diffuse emission as it is located along the Galactic plane. This is the same map from Ackermann et al. (2016, see Figures 1 and 5). The angular diameter in radio of the SNR is indicated in cyan, and the 95% uncertainty position of the 2FHL source is marked by the dashed magenta circle.

estimated to be 6.3 kpc from HI absorption measurements. Yamaguchi et al. (2012) argue that 6.3 kpc is far too close given the high absorbing column density, N_{H} , measured in the direction of the SNR in the X-ray and must be at least as far as the Galactic tangent point of 8 kpc. Considering the uncertainty of the SNR distance, we adopt the far and near distances of 14 and 6.3 kpc, respectively, throughout this paper.

The location of the SNR is coincident with a high-density region with plumes of CO, neutral hydrogen, and dust (noticed by abundant IR emission at $24 \mu\text{m}$) surrounding the SNR radio shell (Giacani et al. 2011). Because of the local medium’s tumultuous environment in this region, it has been suggested that the increased radio surface brightness and observed IR emission to the west of the remnant indicates that it is interacting with the ambient interstellar medium (ISM; Combi et al. 2010; Giacani et al. 2011; Chawner et al. 2019). It would seem plausible then for the SNR to be the result of a core-collapse (CC) supernova (SN) explosion as these cloudy, dense environments indicate a massive star exploded not far from its original birthplace. However, the stellar progenitor of this system is yet to be firmly identified because no compact remnant has been identified within the SNR to date that challenges the CC origin theory (Combi et al. 2010; Giacani et al. 2011; Yamaguchi et al. 2012). Combi et al. (2010) attempted to tie the unresolved compact X-ray source detected by both XMM-Newton and Chandra, CXOU J170357.8–414302, to the SNR due to its positional overlap with the center of the remnant. However, the characteristics of the potential central compact object (CCO) in the optical and infrared fit more with a K0-dwarf star in the foreground. The CCO also requires a drastically different absorbing column density than what is estimated for the SNR.

Other attempts to classify SNR G344.7–0.1 as a CC SN include Chang et al. (2008), where an X-ray study was performed to try to identify the extended dark TeV source, HESS J1702–420, as the PWN around the pulsar, PSR J1702–4128, that could be a displaced progenitor of the SNR. If this could be confirmed, it would be a persuasive argument that the SNR descended from a CC SN explosion; however, results from Chang et al. (2008) are inconclusive. It is also worth mentioning that the estimated age of

PSR J1702–4128 is 55 kyr with a distance of $d \approx 5.2$ kpc, whereas the SNR is ~ 3000 yr old³ (Giacani et al. 2011) and is at least 6.3 kpc away (Giacani et al. 2011; Yamaguchi et al. 2012). Therefore, this scenario is unlikely.

Yamaguchi et al. (2012) suggest this SNR is more likely the result of a type Ia SN, based on strong Fe K-shell emission detected in the X-rays (6–7 keV) likely emitted from the SN ejecta. Fe emission is frequently observed among type Ia SNRs, while it would be unusual to be found in CC SNRs (Yamaguchi et al. 2012). For this reason, we could indeed be viewing a unique case of a type Ia SNR interacting with a dense, inhomogeneous surrounding medium.

This paper describes the analysis of existing X-ray observations of the SNR in the region coincident with 2FHL J1703.4–4145, as well as archival multiwavelength data in the region where 2FHL 1703.4–4145 is located, how the dark TeV source HESS J1702–420 may play a role in this region, and the modeling of the broadband spectral energy distribution to better understand the origin of the observed γ -ray emission.

1.2. HESS J1702–420

Extended and yet unidentified source, HESS J1702–420, located at (R.A., decl.) = $(255^{\circ}63, -42^{\circ}07) \pm 0^{\circ}05$ in J2000, is a likely TeV counterpart of 2FHL J1703.4–4145 due to their positional coincidence with SNR G344.7–0.1 and compatible γ -ray spectral energy distributions (see Figure 1).

As previously mentioned, HESS J1702–420 was briefly investigated as a possible displaced PWN to an unseen pulsar or to a detected but displaced pulsar (e.g., PSR J1702–4128 in Chang et al. 2008) associated with the SNR; however, the results remain inconclusive and the nature of the TeV source is still unknown.

A second possibility explaining the extended TeV emission with its peak seen unusually far from the SNR could be runaway CR diffusion that is hitting a nearby molecular cloud

³ This estimate is based on the ionization timescale τ/n_e , taking $n_e \sim 1 \text{ cm}^{-3}$ of the observed X-ray emission.

and illuminating it. This hypothesis seems plausible based on observationally constrained Monte Carlo simulations (Cui et al. 2016). It would also explain the GeV γ -ray emission observed with Fermi-LAT as mainly the result of leaked GeV CRs from a shock–cloud collision with a molecular cloud core (Cui et al. 2019). In summary, the displaced TeV emission from an SNR can be described by runaway TeV CRs released early on from the SNR that diffuse rapidly and travel distances of 10–100 pc. Meanwhile, the GeV CRs escape and diffuse slower and will be mostly concentrated at the shock–cloud boundary.

If HESS J1702–420 is indeed the TeV counterpart of 2FHL J1703.4–4145 as the SED suggests (see Figure 1), and both are associated to SNR G344.7–0.1, a possible scenario is one where the SNR is interacting with a cloud at the western boundary, explaining the concentration of GeV emission at the location of 2FHL J1703.4–4145. Subsequently, HESS J1702–420 could be explained by a dense cloud located at the TeV source position being penetrated and illuminated by runaway TeV CRs that escaped from the SNR at an earlier time.

On the contrary, Lau et al. (2019) consider the same scenario in which CRs are accelerated by the SNR, diffuse into the ISM, and thus generate HESS J1702–420 as the CRs interact with a molecular cloud here. The authors find CR escape and diffusion into a nearby cloud to be an unlikely explanation for the TeV source, determined by using a diffusion time relationship from Ginzburg & Syrovatsky (1965). The results suggest the diffusion time for escaped CRs to be much greater than the SNR age. However, we point out that the estimates by Lau et al. (2019) are far too large, both the derived diffusion times and SNR ages. Lau et al. (2019) use the diffusion coefficient equation from Gabici et al. (2007); however, this derivation only considers existing clouds embedded in the diffuse Galactic cosmic-ray population and does not account for a local CR accelerator like an SNR. In fact, Gabici et al. (2009) derive the diffusion coefficient considering both the diffuse Galactic CR flux and the contribution of CRs from a local CR accelerator, specifically of an SNR. The coefficients are more than a magnitude in difference when accounting for SNR-accelerated CRs; therefore, the improved estimate for the diffusion coefficient is

$$D(E) = 10^{28} \left(\frac{E}{10 \text{ GeV}} \right)^{0.5} \text{ cm}^2 \text{ s}^{-1}, \quad (1)$$

where E is the CR energy. We also invoke the relationship from Ginzburg & Syrovatsky (1965) of $\tau_{\text{diff}} = \frac{d^2}{6D(E)}$, where d is the distance to the TeV emission peak from the SNR, corresponding to $d \sim 120$ pc and $d \sim 55$ pc in the 14 kpc and 6.3 kpc SNR distance scenarios, respectively. We use the same CR energy input as Lau et al. (2019), $E_{\text{CR}} = 2$ TeV, that would generate γ -rays with energy ~ 200 GeV, close to the detection threshold of H.E.S.S. Using the diffusion coefficient in (1) instead, the estimated diffusion times become $\tau_{\text{diff}} \approx 5.2$ kyr and $\tau_{\text{diff}} \approx 1.1$ kyr for the estimated SNR distances of 14 kpc and 6.3 kpc, respectively (compared to the estimates of $\tau_{\text{diff}} \approx 100$ kyr and $\tau_{\text{diff}} \approx 34$ kyr; Lau et al. 2019).

We also reestimated the SNR ages using the Sedov–Taylor phase of an SNR (Taylor 1950; Sedov 1959),

$$\left(\frac{t}{100 \text{ yr}} \right)^{\frac{2}{5}} = \frac{R_{\text{sh}}}{2.3 \text{ pc}} \left(\frac{E}{10^{51} \text{ ergs}} \right)^{\frac{1}{5}} \left(\frac{\rho_0}{10^{-24} \text{ g cm}^{-3}} \right)^{-\frac{1}{5}}, \quad (2)$$

where R_{sh} is the shock radius, E is the SN explosion energy, and ρ_0 is the ambient density. At a distance of 14 kpc, $R_{\text{sh}} \sim 16$ pc, and at 6.3 kpc, $R_{\text{sh}} \sim 7$ pc. We assume a ρ_0 corresponding to an ambient particle density of $n_0 = 1 \text{ cm}^{-3}$ and $E_{\text{SN}} = 10^{51}$ ergs. We find that at a distance of 14 kpc, the SNR age would be ~ 10 kyr, and at 6.3 kpc, the SNR age would be ~ 1.2 kyr, significantly lower than the estimates found in Lau et al. (2019).

A third explanation of HESS J1702–420 in association with the SNR could be that it is a TeV halo from a displaced pulsar and a PWN that is yet to be discovered. TeV halos are spatially extended, nonthermal high-energy γ -ray emission surrounding a PWN. TeV halos are much larger in extension than PWNe but are close enough to the central pulsar that this region is still dominated by pulsar activity and cosmic-ray diffusion (Sudoh et al. 2019). The γ -ray emission is produced by escaped ~ 10 TeV electrons and positrons from the termination shock of the PWN, scattering off of the interstellar radiation field. TeV halos are observed to have a hard spectrum in this regime with a photon index ~ 2.2 (Sudoh et al. 2019). HESS J1702–420 is best fit with a power-law index of 2.1 ± 0.1 , in good agreement with TeV halo observations. If this scenario is confirmed, this would indicate SNR G344.7–0.1 as a CC supernova remnant with a clear Fe–K emission line present in the X-ray spectrum, which would be a peculiar finding for a CC SN (Yamaguchi et al. 2012).

This paper is organized as follows: In Sections 2 and 3 we discuss the source selection and the XMM-Newton data reduction and analysis. A further multiwavelength characterization of the source is presented in Section 4. Section 5 explores the depicted scenario through the SED modeling, and Section 6 summarizes our results.

2. Source Selection

2FHL J1703.4–4145 was first detected at >50 GeV in the 2FHL catalog and presents a particularly hard γ -ray spectrum with photon index $\Gamma_\gamma = 1.24 \pm 0.36$ and a maximum photon energy of ~ 1.7 TeV (Ackermann et al. 2016). The source was also detected above 10 GeV and reported in the 3FHL catalog⁴ (see Figure 1). The 3FHL catalog (Ajello et al. 2017) covers a larger energy range from 10 GeV to 2 TeV and adopts a longer exposure of 84 months, compared to the 80 months used in the 2FHL catalog. Furthermore, the 3FHL catalog results from taking full advantage of improvements provided by Pass 8, using the point-spread function (PSF)–type event classification, improving sensitivity and leading to an increase in photon counts 10 times greater than what is reported in the 2FHL catalog. Therefore, the 3FHL counterpart provides us with more information of 2FHL J1703.4–4145 in the high-energy regime. Above $\gtrsim 10$ GeV, the Fermi-LAT PSF is $\sim 0.1^\circ$ at 68% confidence level (C.L.; Ajello et al. 2017). The source is compact and shows no clear evidence of extended emission beyond the PSF of the Fermi-LAT in this energy range.

To further investigate the properties of this VHE object, we performed an X-ray analysis on XMM-Newton archival data

⁴ We will continue to use the 2FHL identifier for 2FHL J1703.4–4145 for two reasons. One being that the 2FHL and 3FHL identifiers and properties for 2FHL J1703.4–4145 are the same and the other being that the subsample this source is a part of was generated using the unidentified objects in the 2FHL catalog as described in Section 1. Any major differences between 2FHL sources in this Galactic sample and subsequent Fermi-LAT catalog counterparts will be addressed in their respective reports.

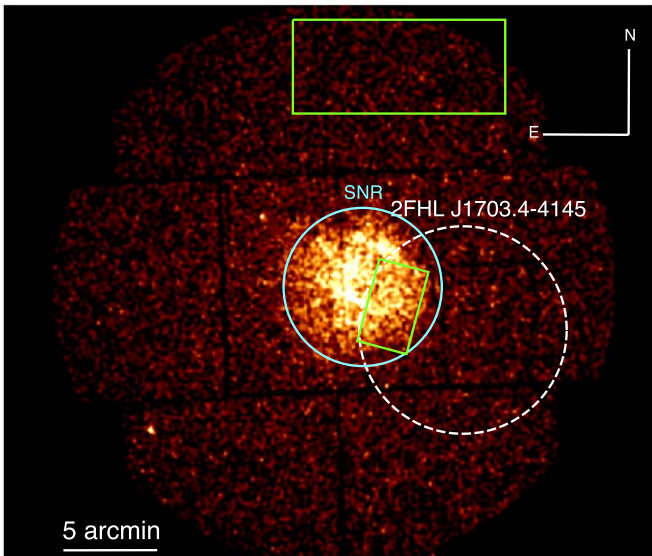


Figure 2. Smoothed MOS2 0.5–10 keV image of SNR G344.7–0.1, which is indicated in cyan. The white dashed circle ($r = 5/2$) represents the 95% positional uncertainty of 2FHL J1703.4–4145. The green box covering the western half of the SNR is used for the source spectrum, and the large green rectangle at the top is used for the background spectrum.

from 2001 (ObsID: 0111210401, PI: M. Watson) in order to better understand which part of the SNR is likely responsible for the γ -ray emission observed.

3. XMM-Newton X-Ray Analysis

3.1. XMM-Newton Data Reduction and Analysis

The entire system of SNR G344.7–0.1 was observed with XMM-Newton in 2001 for 12.2 ks in full frame mode. In Figure 2 we show the smoothed 0.5–10 keV image of SNR G344.7–0.1, as seen with the MOS2 camera mounted on XMM-Newton. Data reduction was performed using SAS software (v17.0) with the corresponding calibration files for XMM-Newton.⁵ In Figure 2, the position of the SNR is indicated using the $8'$ radio angular diameter as well as the location of 2FHL J1703.4–4145 with respect to the SNR. The 2FHL 95% confidence region overlaps the western half of the supernova remnant, which suggests that the γ -ray emission is associated with this object.

The selected regions for the spectral fitting process are indicated in Figure 2. Modeling both the source and background, we perform a spectral fitting on the resulting spectra from MOS1, MOS2, and PN using the HEASOFT software package (v6.19; Drake & Smale 2016) with XSPEC (v12.9.1) in order to find the best model to characterize the observed emission. The background is modeled taking into account both the instrumental and astrophysical contributions. The first is modeled as a combination of quiescent soft protons, CR-induced continuum, and fluorescence lines and the latter is modeled as both the emission from the Galactic halo and the cosmic X-ray background.⁶ The instrumental background component is negligible across the energy range but does account for prominent fluorescence lines including those of

⁵ XMM-Newton calibration files can be found at https://heasarc.gsfc.nasa.gov/docs/xmm/xmmhp_caldb.html.

⁶ For a careful treatment of faint, extended objects using the same background model see Paper Ia and references therein.

Table 1
Summary of the Statistics and Parameters for the Best-fit Model in Our Analysis, *phabs* (*vnei* + Gaussian)

C-stat	d.o.f. ^a	C-stat/d.o.f.
850.22	719	1.18
Component	Parameter	Best-fit Value
<i>phabs</i> ^b	$N_{\text{H}}(10^{22} \text{ cm}^{-2})$	$6.81^{+1.03}_{-1.20}$
<i>vnei</i>	$kT(\text{keV})$	$1.33^{+0.34}_{-0.22}$
	Mg	< 0.83
	Si	$2.70^{+1.01}_{-0.91}$
	S	$3.10^{+0.76}_{-0.44}$
	Ar	$3.00^{+0.63}_{-0.58}$
	Ca	$5.40^{+1.66}_{-1.35}$
	$\tau (10^{11} \text{ cm}^{-3} \text{ s})$	$1.05^{+0.35}_{-0.26}$
Fe	$E(\text{keV})$	$6.47^{+0.048}_{-0.045}$
	$\sigma (\text{keV})$	$0.12^{+0.070}_{-0.050}$
	Normalization	$3.86^{+1.23}_{-1.03} \times 10^{-5}$

Notes. Metal abundances are reported in solar units.

^a Degrees of freedom.

^b Absorption cross section set to Verner et al. (1996).

Al–K (~ 1.5 keV), Si–K (~ 1.8 keV), Cr–K (5.4–5.9 keV), Mn–K (~ 5.9 keV), and Fe–K (~ 6.4 keV). We binned the spectrum at 25 counts per bin and used the C-stat statistic.

3.2. Spectral Analysis Results

SNR G344.7–0.1 has been studied in the X-rays in Combi et al. (2010), Giacani et al. (2011), Yamaguchi et al. (2012), and Fukushima et al. (2020), all finding that thermal models can describe the entire remnant appropriately. Using this as a starting point for our spectral analysis, we found that the *vnei* model (Hamilton et al. 1983) best describes the spectrum from the western half of the SNR. The *vnei* model characterizes a nonequilibrium, ionized, and collisional plasma that is constant in temperature and allows the ionization timescale to vary. The best-fit parameters for the model are reported in Table 1, and the best-fit model is shown in Figure 3. There are several metal emission lines present, including Mg (~ 1.5 keV), Si (~ 1.7 keV), S (~ 2.4 keV), Ar (~ 2.5 keV), Ca (~ 4 keV), and Fe (~ 6.4 keV). These findings are consistent with previous works (Yamaguchi et al. 2012; Fukushima et al. 2020), and the Fe emission observed in the spectrum supports the scenario where the SNR may result from a type Ia SN (Yamaguchi et al. 2012).

The emission lines are modeled using *vnei* where available, but we find a Gaussian component can better model one of these emission lines and provide overall better statistics. The feature to require additional modeling is the Fe–K α line at 6.4 keV as this is not well modeled with *vnei*, likely due to this arising from another plasma component with a different ionization timescale (Yamaguchi et al. 2012; Fukushima et al. 2020).

We find the best fit for the observed X-ray spectrum to be an absorption component *phabs* (Arnaud 1996) multiplying *vnei* and a Gaussian. The solar abundances are assumed to be the Wilms et al. (2000) ones. The *vnei* parameters H, He, C, N, and O are set to unity, following Yamaguchi et al. (2012). Our results are consistent with Giacani et al. (2011) using the same observation from XMM-Newton and the same model.

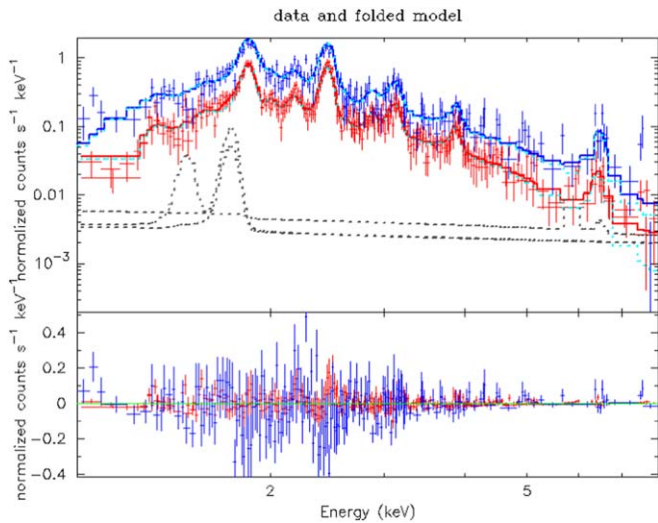


Figure 3. Top: XMM-Newton MOS1 and MOS2 (red), and pn (blue) data of the source and background regions (see Figure 2) and the best-fit model (blue and red solid lines) obtained using `phabs(vnei + Gaussian)`. The emission lines observed between 1 keV and 7 keV correspond to metals in the plasma: Mg (~ 1.5 keV), Si (~ 1.7 keV), S (~ 2.4 keV), Ar (~ 2.5 keV), Ca (~ 4 keV), and Fe (~ 6.4 keV), which is consistent with the results reported in Giacani et al. (2011), Yamaguchi et al. (2012), and Fukushima et al. (2020). The dotted dark gray lines correspond to the instrumental background contributions for each data set. The dashed cyan lines correspond to the combination of source and astrophysical background contributions. Bottom: residual map of the data and best-fit model.

However, comparing the X-ray data from XMM-Newton to Suzaku and Chandra X-ray data (Yamaguchi et al. 2012; Fukushima et al. 2020) shows that the Fe line cannot be attributed to background fluorescence alone as a Fe K line is clearly detected in all data sets. We have carefully modeled the background, including the Fe $K\alpha$ fluorescence at 6.4 keV. Significant Fe emission from the SNR is apparent and is therefore included in the source model. Contributions from both background and source emission are plotted separately in Figure 3. N_{H} values reported here are slightly higher than previous works (Giacani et al. 2011; Yamaguchi et al. 2012) and this is due to assuming Wilms et al. (2000) abundances as in Fukushima et al. (2020). Finally, we note the supersolar abundances of the metals, with the exception of Mg, indicating this emission is from a mixture of shocked SN ejecta and swept-up ISM, similarly found in Giacani et al. (2011), Yamaguchi et al. (2012), and Fukushima et al. (2020).

4. Multiwavelength Information

4.1. Radio

Central emission within the shell is clearly visible in many radio bands including 408 and 5000 MHz (Clark et al. 1975), 1465 MHz (Dubner et al. 1993; Giacani et al. 2011), 115 GHz (^{12}CO ; Giacani et al. 2011), 1.4 GHz (ATCA and VLA; Giacani et al. 2011), and 843 MHz (see Figure 4).

Dubner et al. (1993) described the SNR in 1465 MHz as having a revealing shell morphology and reported for the first time the detection of bright central emission indicating the remnant to be a composite SNR type. Dubner et al. (1993) also provided the first linear diameter and distance estimations of $D \approx 33$ pc and $d \approx 14$ kpc based on the $\Sigma - D$ calibration technique from Huang & Thaddeus (1985). This technique is not very reliable due to large intrinsic dispersion (see, e.g.,

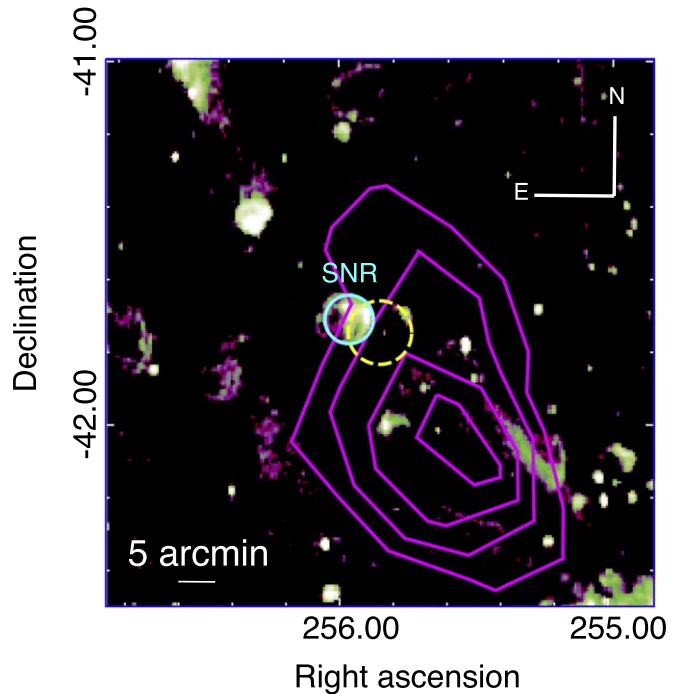


Figure 4. Molonglo Observatory Synthesis Telescope (MOST) 843 MHz map from Whiteoak & Green (1996) where the SNR shell of $8'$ is readily seen and marked by the solid cyan circle with the 95% confidence region of 2FHL J1703.4-4145 indicated by the yellow dashed circle. We plot HESS J1702-420 flux contours from H.E.S.S. Collaboration et al. (2018) to show where the emission peak is located. We note that the bright anomaly just within the northwest corner of the Fermi-LAT uncertainty region is more than likely a young stellar object and not associated to the observed γ -ray emission (see the text).

Dubner et al. 1993; Yamaguchi et al. 2012, and references therein), but is considered a conservative distance estimate for the SNR to date (Yamaguchi et al. 2012).

As can be seen in Figure 4, the western and central part of the SNR are much brighter than the eastern half. 1.4 GHz data from the Australia Telescope Compact Array (ATCA) and the Very Large Array (VLA) reveal the shell to be nearly complete with a diameter of $8'$ (Giacani et al. 2011). The observed central X-ray emission (Figure 2) is totally encompassed by the radio shell. Furthermore, the radio surface brightness is also seemingly correlated to the IR emission that peaks to the west as well at $24 \mu\text{m}$ (e.g., see Figure 5).

A shock-cloud interaction is a preferred scenario to explain the bright central radio emission as well as other enhanced emission (Combi et al. 2010; Giacani et al. 2011). This is supported by the broad presence of both neutral hydrogen and carbon monoxide⁷ (Giacani et al. 2011; Lau et al. 2019; Fukushima et al. 2020).

We note that the bright anomaly just within the northwest corner of the 95% Fermi-LAT uncertainty region (see Figures 4 and 5) is more than likely a young stellar object (YSO) and not associated to the observed γ -ray emission.⁸

⁷ Public data for the Mopra CO survey data release 3 can be found at <https://doi.org/10.7910/DVN/LH3BDN> and was first reported in Braiding et al. (2018).

⁸ This anomaly is bright in both the radio and IR and is coincident with an H II region (HRDS G344.593-00.044), a submillimeter YSO (AGAL G344.606-0.031), and a large H II bubble (SPK2012 MW1G344590-00500), and therefore is more than likely unrelated to the SNR and consequently the 2FHL source.

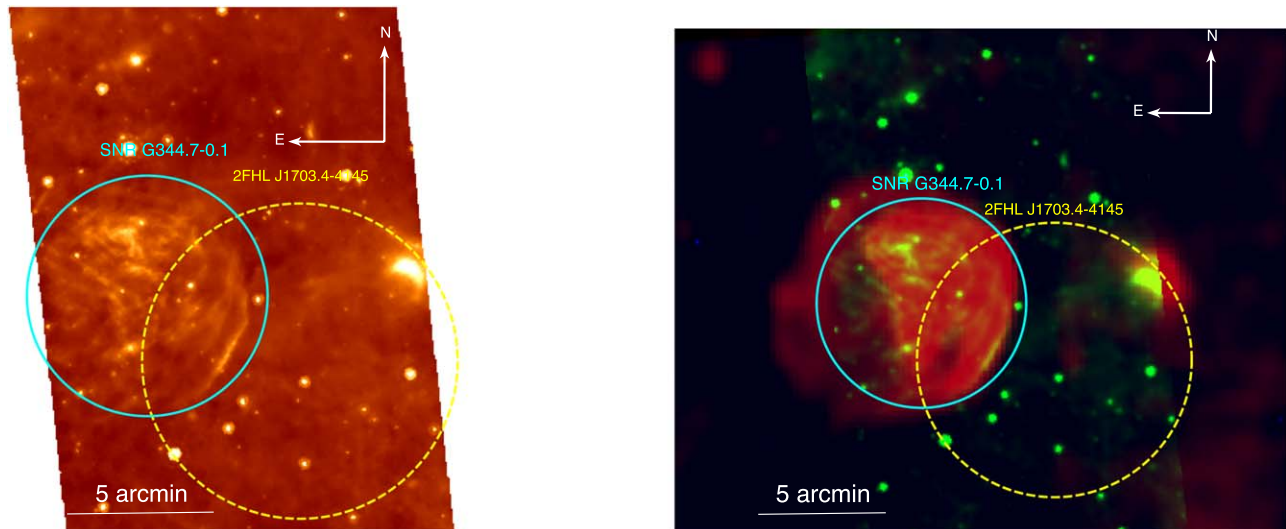


Figure 5. Left: SPITZER 24 μm image of SNR G344.7–0.1 with 2FHL J1703.4–4145 95% uncertainty region indicated. Note the bright filament on the western edge of the SNR that overlaps well into the 2FHL region. Right: 843 MHz (red) superposed with 24 μm (green) and 8 μm (blue) SPITZER MIPS and IRAC images, respectively. The bright radio emission is paired with bright IR emission in the center of the SNR. A bright IR filament traces the western edge of the SNR, coincident with the position of 2FHL J1703.4–4145. These two points indicate an interaction between the remnant and its surroundings.

4.2. Infrared

Spitzer GLIMPSE survey data of SNR G344.7–0.1 at 24 μm are shown in Figure 5 (left panel). It is reported in Andersen et al. (2011) that the SNR exhibits several features in the IR band that are indicative of an interaction between the SNR shock wave and its dense surroundings.

The IR image at 24 μm provides indicators of shocked dust being swept up by the forward shock of the remnant as it expands into the ISM. The IR filament observed to the west of the remnant shell and well within the 2FHL uncertainty region could indicate where a shock–cloud interaction is occurring that may be accelerating particles to cosmic-ray energies. To support this claim, there is an abundance of gas, particularly HI, in the region of the SNR that could provide a dense medium for the forward shock to run into (see Section 4.1 and Combi et al. 2010; Giacani et al. 2011; Yamaguchi et al. 2012; Lau et al. 2019). Moreover, it has been discovered that a bright X-ray filament in the 1.76–1.94 keV energy range as seen with Chandra coincides with the IR filament (Fukushima et al. 2020). However, it is suggested to be of SN ejecta origin rather than a forward shock front propagating into the ISM due to the relative abundances of S, Ar, Ca, and Si being comparable to solar values accompanied by a much lower presence of Mg. On the other hand, other recent work describes the dust features being consistent with a non-SN origin (i.e., swept-up material; see Chawner et al. 2019, 2020).

Moreover, there is enhanced mid-IR emission from shocked ionized gas that coincides with the bright radio central emission (Chawner et al. 2019). IR emission is also detected in the north as well, pointing to an interaction between the supernova shock and a molecular cloud in front of the SNR (Chawner et al. 2019).

4.3. Soft X-Rays

In the soft X-rays, SNR G344.7–0.1 is encompassed with thermal emission across the remnant within the radio shell as seen with XMM-Newton, Chandra, Suzaku, and ASCA (see Section 4.2, Figure 2, and Yamauchi et al. 2005; Combi et al. 2010;

Giacani et al. 2011; Yamaguchi et al. 2012; Fukushima et al. 2020). The temperature of the SNR is roughly $kT \sim 1.0$ –1.5 keV across the remnant (see Section 3 and Combi et al. 2010; Giacani et al. 2011; Yamaguchi et al. 2012; Fukushima et al. 2020). Specifically in this work, the X-ray emission overlapping with the observed γ -ray emission is found to have a temperature $kT = 1.33^{+0.34}_{-0.22}$ keV at 90% C.L.

5. Discussion

5.1. Efficient Particle Acceleration

SNRs are widely thought to accelerate a significant fraction of Galactic CRs through diffusive shock acceleration (DSA) in their high-velocity blast waves. The γ -ray emission in the MeV–GeV band from regions with relatively high ambient density is expected to be hadronic in origin (see Castro et al. 2013a and Figure 6 for an example), and hence evidence of CR hadron acceleration at these shocks. Proton–proton collisions between shock-accelerated CR ions and ambient protons are enhanced in high-density regions such as an interaction between an SNR forward shock and a molecular cloud or a CR accelerator located near a high-density cloud. The energetics of 2FHL J1703.4–4145 make this site another promising source for efficient particle acceleration to CR energies. The best-fit physical parameters for both leptonic and hadronic emission scenarios are investigated in Section 5.2.

The X-ray band may also provide clues. Where the shock has become radiative, it is likely to become bright in the GeV band, such as W44 and IC 443, and the resulting X-ray emission is commonly characterized by a center-filled X-ray morphology, rather than a shell-like one, similar to what is observed for SNR G344.7–0.1 (Slane et al. 2015). Generally bright optical filaments that are associated with thermal X-ray emission provide evidence for the shock to still have enough speed to heat the surrounding medium to X-ray emitting temperatures and hence a significant part of the shock could likely be nonradiative. Thus, if bright optical filaments can be discovered in the region of 2FHL J1703.4–4145, then it is possible CRs in this region have been produced through DSA.

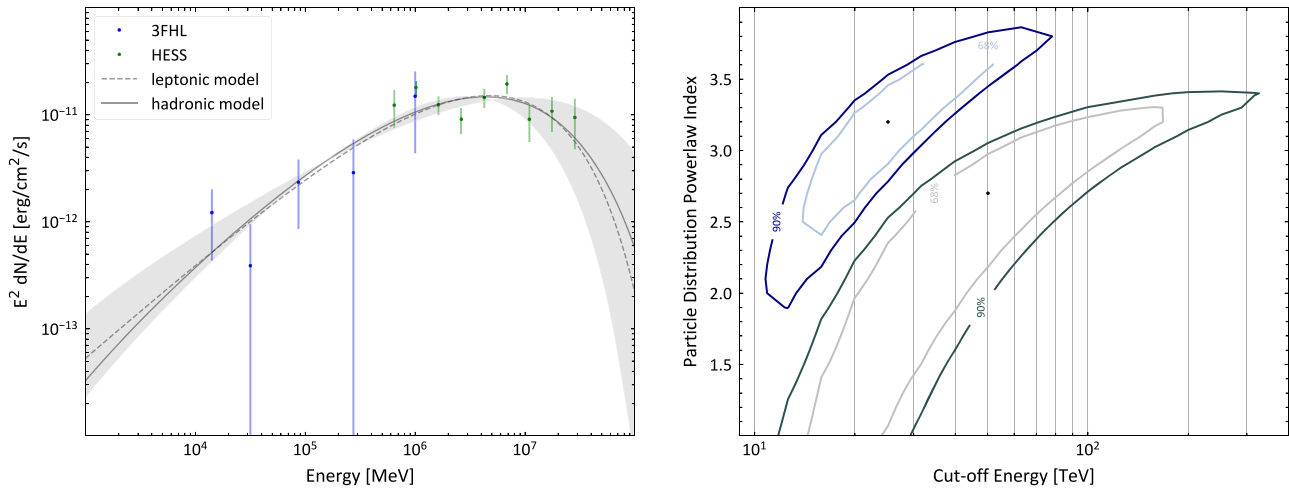


Figure 6. Left: the spectral energy distribution model constrained to 3FHL and HESS spectral data. The solid gray line (hadronic scenario) and the dashed gray line (leptonic scenario) demonstrate the resultant γ -ray spectrum of radiation from relativistic protons or electrons, respectively. Right: IC decay (blue) and pion decay (gray) model contour plot for the spectral fitting results, marking the 1σ and 2σ uncertainties. The black dot shows the best-fit values. The best-fit values are listed in Table 2.

5.2. Modeling Spectral Energy Distribution

The multiwavelength information available can be combined to build a picture of the broadband spectral characteristics of the region. Assuming the GeV γ -ray emission of 2FHL J1703.4–4145 is indeed the result of radiation from a relativistic particle population accelerated by the SNR G344.7–0.1 shock, it is possible to model the broadband emission from the shock-accelerated nonthermally distributed electrons and protons and hence derive constraints on the physical parameters of the mechanism responsible for the observed emission.

We assume the distribution of the accelerated particles in momentum to be

$$\frac{dN_i}{dp} = a_i p^{-\alpha_i} \exp\left(-\frac{p}{p_{0i}}\right). \quad (3)$$

Here, subindex i represents the particle type (proton or electron), and α_i and p_{0i} are the spectral index and the exponential cutoff momentum of the distributions. The coefficients for the particle distributions, a_p and a_e , are set using the total energy in relativistic particles and the electron-to-proton ratio as input parameters, together with the spectral shape of the distributions. The spectral indices of electron and proton distributions are assumed to be equal, and for the nonthermal radiation from these particle distributions we have used π^0 -decay emission from Kamae et al. (2006) and Mori (2009) and inverse Compton (IC) emission from Baring et al. (1999) and references therein. For more details on the model and application see Castro et al. (2013b) and Paper 1a.

We use the model outlined above to establish the approximate ranges of some of the physical parameters that would result in emission that fits the Fermi-LAT data, as well as complying with available data at other wavelengths. We adopt a distance of $d = 6.3$ kpc. The input parameters for each model considered are included in Table 2, and the resulting SED models are shown in Figure 6 (left panel).

When trying to fit the broadband spectral data, including radio at 1.4 GHz from ATCA (Giacani et al. 2011), X-ray (from Chandra data; ObsID: 21117, PI: Yamaguchi), and γ -ray (from Ajello et al. 2017; H.E.S.S. Collaboration et al. 2018), it

Table 2
SED Input Model Parameters

	p_0 (TeV/c)	Γ_γ	E_{CR} (10^{50} erg (d/6.3 kpc) 2)
Leptonic	25.1	2.2	0.0093
Hadronic	50.1	1.6	4.3

Note. Target density in hadronic model is assumed to be 1 cm^{-3} .

becomes apparent that the radio and X-ray data are not connected to the γ -ray emission mechanism, suggesting that two different electron particle populations are at work. Fitting the multiwavelength data using one electron population requires the magnetic field to be much lower than the average ISM value of $\sim 3 \mu\text{G}$, which is unlikely. Additionally, including the γ -ray data indicates that it is unlikely the CRs responsible for the GeV–TeV emission are trapped in the SNR shock. If this were the case, then considering the typical minimum magnetic field strength in the Galaxy being approximately $\sim 3 \mu\text{G}$ and that it would be compressed by the shock at least by a factor of 4 (compression factor for a normal SNR shock), we would expect to detect a flux of nonthermal X-ray emission larger than allowed by the upper limit we have derived from the XMM-Newton data. The only scenario that fits the radio, X-ray, and γ -ray data is one where the γ -ray emission is a result of CRs at the SNR shock where the local density is in the order of $\sim 1000 \text{ cm}^{-3}$, which is ruled out by the bright thermal X-ray emission at the shock. If the density were this high, the shock would have rapidly become radiative, and thermal X-ray emission would have declined significantly. Therefore, we show only the spectral model and data that we are able to fit in Figure 6.

Any synchrotron radiation from the relativistic electrons at the SNR shock interacting with the local shock-compressed magnetic field is hidden by the bright thermal X-ray emission from this remnant. Hence, we added a power-law component to the X-ray emission model to estimate an upper limit from the nonthermal component. The upper limit on the flux is $F_X \leq 5.4 \times 10^{-12} \text{ erg cm}^{-2} \text{ s}^{-1}$ for the range 0.2–10 keV.

With the current data, we can determine the inverse Compton (IC) decay maximum cutoff energy at 63.1 TeV and a minimum at 12.6 TeV. The corresponding spectral indices are 3.8 and 1.9, respectively. The maximum spectral index for the pion decay model is 3.4 with an upper limit on the cutoff energy of 316.2 TeV (see Figure 6, right panel). Additionally in the pion decay model, we must impose a minimum spectral index of 2.5 (in momentum, or 1.5 in energy) because no acceleration process is believed to produce harder momentum (or energy) distributions than this. As a result, the minimum cutoff energy is unconstrained.

Using the minimum spectral index of 2.5 in momentum, the minimum CR energy for electrons that could explain the observed γ -ray emission is $5.56 \times 10^{47} \text{ erg}(d/6.3 \text{ kpc})^2$. The maximum CR energy for electrons is $1.74 \times 10^{49} \text{ erg}(d/6.3 \text{ kpc})^2$, considering both distance estimates derived from Dubner et al. (1993) and Giacani et al. (2011) of 14 kpc and 6.3 kpc, respectively. The maximum CR electron energy corresponds to a spectral index of 4.2 in momentum and a cutoff of 200 TeV. The total energy for CR protons, on the other hand, is better bound with a target density of 1 cm^{-3} . The minimum CR energy for protons is $4.0 \times 10^{50} \text{ erg}(n/1 \text{ cm}^{-3})(d/6.3 \text{ kpc})^2$ and a minimum energy of $4.8 \times 10^{50} \text{ erg}(n/1 \text{ cm}^{-3})(d/6.3 \text{ kpc})^2$.

Based on the physical parameters of the best-fit SED models, both the leptonic and hadronic mechanisms could explain the observed γ -ray emission. If the GeV and TeV emission are generated from IC decay, it needs to either be unrelated to the SNR completely or the synchrotron population would need to be responsible for the IC γ -ray emission. However, as can be seen in Figure 2, there is no significant X-ray emission, thermal or nonthermal, that is detected beyond the SNR shell, suggesting no leptonic emission extending far beyond the SNR that poses a problem in explaining the large extension of HESS J1702–420 and its emission peak occurring so far from the SNR. The other possibility would be two particle populations: one population of diffusing hadronic CRs that are escaping into the dense surroundings generating pion decay and the second population generating synchrotron radiation that is observed largely in radio. Because there is no hint of leptonic emission occurring outside of the SNR, the likely scenario is one where hadronic CRs are accelerated at the SNR forward shock where compact GeV emission is observed and escape into the surroundings where the CRs interact with a molecular cloud, generating the observed TeV emission. This is a plausible explanation since the SNR is known to be in a dense region of the Galaxy, though no known molecular cloud (MC) at the position of the TeV emission shows a convincing correlation. If a molecular cloud exists and is being bombarded by the SNR CRs, the molecular cloud would rapidly thermalize and produce X-rays and, as previously mentioned, no thermal X-ray emission is detected beyond the SNR, though this is not unusual if the interaction is relatively new.

6. Conclusions

The discovery and investigation of VHE γ -ray emission to the west of SNR G344.7–0.1 are presented. Multiwavelength data seem to point toward 2FHL J1703.4–4145 originating from SNR CRs accelerated by the forward shock that diffused into the ISM and interacted with a nearby molecular cloud, explaining the observed TeV emission, HESS J1702–420. If this is the case, SNR G344.7–0.1 would be a candidate for fresh CR acceleration. We perform and report a broadband

spectral fitting and find that the γ -ray emission could be explained by either leptonic or hadronic scenarios; however, a pion decay scenario seems most likely based on the lack of leptonic emission seen beyond the SNR in the radio and X-ray.

The presence of a large MC coincident with the observed γ -ray emission or other tracers of an SNR–MC interaction like those mentioned in Paper Ia (see Sections 4.1 and 4.3) would be able to better determine the likelihood of the SNR freshly accelerating CRs. A deeper analysis in the VHE regime using instruments like Fermi-LAT, H.E.S.S., and the Cherenkov Telescope Array (CTA)⁹ would ultimately improve our understanding of what emission mechanism is responsible for what is observed and thus the probability of freshly accelerated CRs in the SNR region.

We acknowledge funding under NASA contract 80NSSC18K1716.

ORCID iDs

J. Eagle  <https://orcid.org/0000-0001-9633-3165>
 D. Castro  <https://orcid.org/0000-0002-0394-3173>
 M. Ajello  <https://orcid.org/0000-0002-6584-1703>

References

- Ackermann, M., Ajello, M., Atwood, W. B., et al. 2016, *ApJS*, **222**, 5
 Aharonian, F., Akhperjanian, A. G., Bazer-Bachi, A. R., et al. 2006, *ApJ*, **636**, 777
 Ajello, M., Atwood, W. B., Baldini, L., et al. 2017, *ApJS*, **232**, 18
 Andersen, M., Rho, J., Reach, W. T., Hewitt, J. W., & Bernard, J. P. 2011, *ApJ*, **742**, 7
 Arnaud, K. A. 1996, in ASP Conf. Ser. 101, *Astronomical Data Analysis Software and Systems V*, ed. G. H. Jacoby & J. Barnes (San Francisco, CA: ASP), 17
 Atwood, W. B., Baldini, L., Bregeon, J., et al. 2013, *ApJ*, **774**, 76
 Baring, M. G., Ellison, D. C., Reynolds, S. P., Grenier, I. A., & Goret, P. 1999, *ApJ*, **513**, 311
 Barrio, J. A. & CTA Consortium 2020, *NIMPA*, **952**, 161588
 Bernlöhner, K., Carrol, O., Cornils, R., et al. 2003, *Aph*, **20**, 111
 Braiding, C., Wong, G. F., Maxted, N. I., et al. 2018, *PASA*, **35**, e029
 Castro, D., Lopez, L. A., Slane, P. O., et al. 2013a, *ApJ*, **779**, 49
 Castro, D., Slane, P., Carlton, A., & Figueroa-Feliciano, E. 2013b, *ApJ*, **774**, 36
 Chang, C., Konopelko, A., & Cui, W. 2008, *ApJ*, **682**, 1177
 Chawner, H., Gomez, H. L., Matsuura, M., et al. 2020, *MNRAS*, **493**, 2706
 Chawner, H., Marsh, K., Matsuura, M., et al. 2019, *MNRAS*, **483**, 70
 Cherenkov Telescope Array Consortium, Acharya, B. S., Agudo, I., et al. 2019, *Science with the Cherenkov Telescope Array* (Singapore: World Scientific)
 Clark, D. H., Caswell, J. L., & Green, A. J. 1975, *AuJPA*, **37**, 1
 Combi, J. A., Albacete Colombo, J. F., López-Santiago, J., et al. 2010, *A&A*, **522**, A50
 Cui, Y., Pühlhofer, G., & Santangelo, A. 2016, *A&A*, **591**, A68
 Cui, Y., Yang, R., He, X., Tam, P. H. T., & Pühlhofer, G. 2019, *ApJ*, **887**, 47
 Drake, S. A., & Smale, A. P. 2016, *AAS/HEAD Meeting*, **15**, 116.16
 Dubner, G. M., Moffett, D. A., Goss, W. M., & Winkler, P. F. 1993, *AJ*, **105**, 2251
 Eagle, J., Marchesi, S., Castro, D., et al. 2019, *ApJ*, **870**, 35, (Paper Ia)
 Eger, P. 2015, *JPhCS*, **632**, 012036
 Ferenc, D. & MAGIC Collaboration 2005, *NIMPA*, **553**, 274
 Fukushima, K., Yamaguchi, H., Slane, P. O., et al. 2020, *ApJ*, **897**, 62
 Funk, S. 2005, *ICRC (Pune)*, **4**, 123
 Gabici, S., Aharonian, F. A., & Blasi, P. 2007, *Ap&SS*, **309**, 365
 Gabici, S., Aharonian, F. A., & Casanova, S. 2009, *MNRAS*, **396**, 1629
 Giacani, E., Smith, M. J. S., Dubner, G., & Loiseau, N. 2011, *A&A*, **531**, A138
 Ginzburg, V. L., & Syrovatsky, S. I. 1965, *ICRC*, **1**, 53
 Hamilton, A. J. S., Sarazin, C. L., & Chevalier, R. A. 1983, *ApJS*, **51**, 115
 H.E.S.S. Collaboration, Abdalla, H., Abramowski, A., et al. 2018, *A&A*, **612**, A1

⁹ See Cherenkov Telescope Array Consortium et al. (2019).

- Holder, J., Atkins, R. W., Badran, H. M., et al. 2006, *APh*, **25**, 391
- Huang, Y. L., & Thaddeus, P. 1985, *ApJL*, **295**, L13
- Kamae, T., Karlsson, N., Mizuno, T., Abe, T., & Koi, T. 2006, *ApJ*, **647**, 692
- Kargaltsev, O., Rangelov, B., & Pavlov, G. G. 2013, arXiv:1305.2552
- Lau, J. C., Rowell, G., Voisin, F., et al. 2019, *MNRAS*, **483**, 3659
- Mori, M. 2009, *APh*, **31**, 341
- Ong, R. A. 2014, *AdSpR*, **53**, 1483
- Renaud, M. 2009, arXiv:0905.1287
- Sedov, L. I. 1959, *Similarity and Dimensional Methods in Mechanics* (New York: Academic)
- Slane, P., Bykov, A., Ellison, D. C., Dubner, G., & Castro, D. 2015, *SSRv*, **188**, 187
- Sudoh, T., Linden, T., & Beacom, J. F. 2019, *PhRvD*, **100**, 043016
- Taylor, G. 1950, *RSPSA*, **201**, 159
- Verner, D. A., Ferland, G. J., Korista, K. T., & Yakovlev, D. G. 1996, *ApJ*, **465**, 487
- Whiteoak, J. B. Z., & Green, A. J. 1996, *A&AS*, **118**, 329
- Wilms, J., Allen, A., & McCray, R. 2000, *ApJ*, **542**, 914
- Yamaguchi, H., Tanaka, M., Maeda, K., et al. 2012, *ApJ*, **749**, 137
- Yamauchi, S., Ueno, M., Koyama, K., & Bamba, A. 2005, *PASJ*, **57**, 459